

High sensitivity photonic time-stretch electro-optic sampling of terahertz pulses

C. Szawaj,^{1,2} C. Evain,^{1,2} M. Le Parquier,² P. Roy,³ L. Manceron,³ J.-B. Brubach,³ M.-A. Tordeux,³ and S. Bielawski^{1,2, a)}

¹⁾Laboratoire PhLAM, UMR CNRS 8523, Université Lille 1, Sciences et Technologies, 59655 Villeneuve d'Ascq, France

²⁾Centre d'Étude Recherches et Applications (CERLA), 59655 Villeneuve d'Ascq, France

³⁾Synchrotron SOLEIL, L'Orme des Merisiers, Saint-Aubin, BP 48, 91192 Gif-sur-Yvette Cedex, France

(Dated: 26 July 2016)

Single-shot recording of terahertz electric signals has recently become possible at high repetition rates, by using the *photonic time-stretch* electro-optic sampling (EOS) technique. However the moderate sensitivity of time-stretch EOS is still a strong limit for a range of applications. Here we present a variant enabling to increase the sensitivity of photonic time-stretch for free-propagating THz signals. A key point is to integrate the idea presented in Ref. [Ahmed et al., Rev. Sci. Instrum. 85, 013114 (2014)], for upgrading classical time-stretch systems. The method is tested using the high repetition rate terahertz coherent synchrotron radiation source (CSR) of the SOLEIL synchrotron radiation facility. The signal-to-noise ratio of our terahertz digitizer could thus be straightforwardly improved by a factor ≈ 6.5 , leading to a noise-equivalent input electric field below 1.25 V/cm inside the electro-optic crystal, over the 0-300 GHz band (i.e, $2.3 \mu\text{V}/\text{cm}/\sqrt{\text{Hz}}$). The sensitivity is scalable with respect to the available laser power, potentially enabling further sensitivity improvements when needed.

PACS numbers: 41.60.Ap, 29.27.Bd, 05.45.-a

I. INTRODUCTION

The so-called photonic time-stretch technique¹ enables single-shot recording of electric pulses with picosecond resolution²⁻⁵, and high acquisition rates (tens of Mega pulses/seconds or more). The speed of these systems has open the way to “terahertz oscilloscopes” with potential applications including analysis of electric signals, guided millimeter waves⁶, freely propagating terahertz pulses^{7,8}, and relativistic electron bunches⁷⁻⁹. However speed is not the only important parameter of photonic time-stretch digitizers. As for classical oscilloscopes, the sensitivity (i.e., the minimum signal that can be distinguished from noise) also largely determines the range of potential applications that may be expected from photonic time stretch, and specific works have naturally aimed at improving signal-to-noise ratios^{4,10}.

Besides, photonic time-stretch devices share common points with electro-optic sampling systems, which are used in terahertz physics¹¹⁻¹⁶ and accelerator physics¹⁷⁻²¹. Hence photonic time stretch and electro-optic sampling can benefit from the advances from each other.

Here we show that it is possible to design photonic systems that combine: (i) the ultra-high sensitivity which is available in recent state-of-art electro-optic sampling^{22,23}, with (ii) the high repetition rate that is characteristic of photonic time-stretch¹. More specifically, we provide guidelines for increasing the sensitivity of pho-

tonic time-stretch setups employing a polarization modulation scheme^{4,7}. We test the efficiency of the strategy for the characterization of terahertz coherent synchrotron radiation (CSR) in the SOLEIL synchrotron radiation facility^{7,24-27}.

II. EXPERIMENTAL STRATEGY

A. Brief review of related photonic time-stretch and electro-optical sampling concepts

In order to record free-space terahertz wave electric fields with high repetition rates and high sensitivity, our experimental strategy is based on combining several existing concepts, borrowed from photonic time-stretch and terahertz electro-optic sampling:

1. Photonic time-stretch

We use photonic time-stretch¹ which is a technique allowing electric field transients to be recorded with high repetition rates (the general principle is resumed in Fig. 1a). Chirped laser pulses are modulated by the ultrafast electric pulses under investigation. Then the pulses are stretched in a long fiber until their duration is of the order of nanoseconds, and may be recorded by an oscilloscope. If some conditions are met³, the output pulses are replica of the input THz pulses, except they are slowed down by a factor:

$$M = 1 + \frac{L_2}{L_1}, \quad (1)$$

^{a)}Electronic mail: serge.bielawski@univ-lille1.fr

with L_1 and L_2 the lengths of the two fibers.

2. Balanced detection

Electro-optic sampling with *balanced detection* is a well known noise-reduction technique, which is widely used in terahertz time-domain spectroscopy^{11,13,28}. Association of photonic time-stretch with balanced detection has been thus naturally implemented in several stups^{4,7}, and a conceptual illustration is presented in Figure 1b. In practice, a quarter-wave plate is placed before the polarizing beam-splitter, and equal powers are sent to the two balanced detector inputs. This technique is particularly efficient for decreasing the common mode noise (as laser relative intensity noise, and amplified spontaneous emission noise of amplifiers placed before the Pockels crystal).

3. Sensitivity increase using near-zero transmission point

In order to increase the sensitivity, a well-known approach consists in operating the set of polarizing elements *near zero transmission point*, e.g., placing the electro-optic crystal between near-crossed polarizers^{29,30}. An association of this technique with photonic time-stretch is presented in Figure 1c. The responsivity (i.e., the laser power modulation amplitude per V/cm electric field) can be increased by orders of magnitude, if a large power is available. This strategy is widely used in single-shot diagnostics of electron bunches in electron accelerators and Free-Electron Lasers^{17,20,21,31}. Note however that associating this technique with balanced detection is not straightforward.

4. Balanced detection and high sensitivity

A further advance has been made recently, when Ahmed, Savolainen and Hamm^{22,23} proposed a compact scheme that combines the advantages of the two previous methods (i.e., near zero transmission point AND balanced detection). This consists in inserting a partial polarizer (Brewster plates in Refs.^{22,23}) in a classical balanced detection setup. We show here that this technique can be easily associated to a photonic time stretch setup, as is illustrated in Fig. 1d (a more compact setup will be presented in the next section). Theoretically, for a given power on the balanced photodetector, and a given (weak) THz electric field, the output signal of Figure 1d is expected to be larger than Figure 1b's signal by a factor $a = 1/\sqrt{T}^{22}$, with T the power transmission of the Brewster plates set for the s-polarization (assuming perfect optics).

B. Experimental setup

We associated the photonic time stretch method and the Ahmed *et al.* high sensitivity strategy, in the compact system represented in Figure 2. Instead of using two fibers after a polarizing beam splitter (as in Figure 1d), we use a single polarization-maintaining (PM) fiber for stretching the two polarization states. The two components are separated only at the fiber's output, using a fiber polarizing beam splitter (PBS in Figure 2). The stretch factor is $M = 200$, i.e., 6 GHz at the oscilloscope input corresponds to 1.2 THz at the electro-optic crystal.

The orientations of the GaP crystal and of the laser and terahertz polarizations are chosen according to Ref.²⁰, in order to maximize the electric field-induced birefringence (see Figure 2 for details). Note that the electric field induced birefringence is at 45 degrees with respect to the $[-1,1,0]$ axis (i.e., at 45 degrees with respect to the plane of the figure). The GaP crystal length is $d = 5$ mm. The laser is an Orange Ytterbium doped fiber laser from Menlo Systems GMBH, delivering mode-locked pulses at 1030 nm, with ≈ 30 nm width, 20 mW average power, and 88 MHz repetition rate. After selection by a pulse picker, the pulses are amplified using a home-made Ytterbium Doped Fiber Amplifier (YDFA). The YDFA output energy depends on the repetition rate, and is typically of the order of 12 nJ for the results presented hereafter. The laser repetition rate is locked on the 104-th harmonic of the storage ring revolution frequency (846.6 kHz) using an RRE synchronization system from Menlo Systems.

Balanced detection is then performed between the two PBS outputs, using a DSC-R412 amplified balanced detector (photoreceiver) from Discovery Semiconductors, with 20 GHz bandwidth and 2800 V/W gain (specified at 1550 nm). An adjustable delay line, and a variable optical attenuator (VOA) are used for matching the relative delays and powers of the two ports, respectively (see Appendix A for delay adjustment procedure and noise suppression by balanced detection). The signals are acquired using a Lecroy Labmaster 10 Zi oscilloscope, with an (overdimensionned) 36 GHz bandwidth. The data are low-pass filtered to 6 GHz, which corresponds to a band-pass limitation of 1.2 THz at the crystal location (see Appendix for details on the transfer function).

In addition to the laser pulses interacting with the THz signals, extra laser pulses are also generated for providing a dark reference (i.e., without terahertz signal), which is subtracted from the data, at the processing stage.

Tests of the EOS setup are performed using coherent THz pulses that are delivered by the Synchrotron SOLEIL facility, in normal user mode, at the AILES beamline³². The conditions are similar to the ones of Ref.⁷, except that the beam current is lower here (12 mA), and 8 electron bunches are operated simultaneously. Below, we focus on the emission by one of the 8 electron bunches, at a repetition rate of 0.85 MHz.

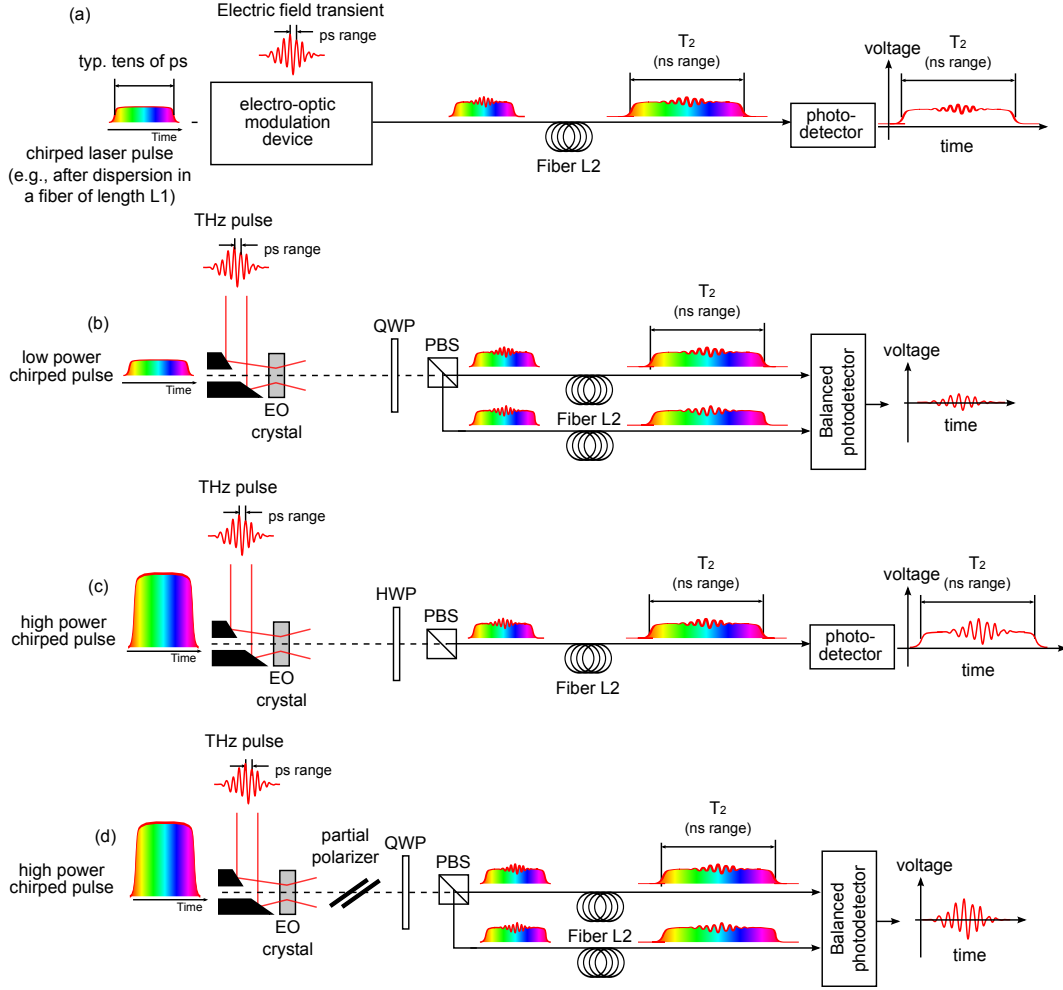


FIG. 1. (a): Illustration of the photonic time stretch technique, and (b-d): possible associations with existing signal-to-noise enhancement techniques. (b): balanced detection, which reduces efficiently the common mode optical noise. (c): Near zero optical transmission point operation, which is particularly efficient for increasing the output electro-optic signal, if a sufficiently high power laser source is used. (d): Association of the three (a, b & c) techniques: Balanced detection and near-zero transmission operation (using the trick from Ref.²²), and photonic time stretch. The detailed (and more compact) setup used in our experiments is displayed in Figure 2. PBS: polarizing beam-splitter. EO crystal: electro-optic crystal.

III. EXPERIMENTAL RESULTS

In Figure 3, we have represented a typical raw single-shot signal, i.e., the signal from the balanced photodetector over a 6 GHz bandwidth. From these data, we can deduce the evolution of the THz electric field value inside the crystal (see Appendix B for details), and the evolution of the THz field-induced birefringence phase shift (Fig. 4).

The terahertz emission occurs in the form of bursts, which are separated by 1.25 ms, and contain several hundreds of THz pulses. The upper parts of Figs. 3, and 4 display recordings used with the present setup, and the lower part displays a reference EOS signal, obtained without the ZnSe plates. Panels a-c represent the same data in different ways: (a) are examples of single-shot signals, (b) and (d) represent series of EOS signals $V_n(t)$ over

many shots n (at 846.6 kHz repetition rate), and (c) is a vertical cut of (b). In both cases (with and without ZnSe plates), the laser power at the EOS setup input has been set as high as possible: (i) just below the detector saturation for the reference without ZnSe plates – i.e., ensuring the best signal to noise ratio (SNR) – and (ii) ≈ 4 times below detector saturation in the setup with ZnSe plates (a value limited by the available amplifier's output power), i.e., leading to a not optimal value for the SNR.

A significant difference in SNR is visible between these two recordings (compare in particular the (b) and (c) panels of the upper and lower data). Remarkably, the SNR is better with ZnSe plates, even though the laser power on the photodiodes is significantly lower. This indicates that further improvement in SNR can even be obtained in the future, just by increasing the output power

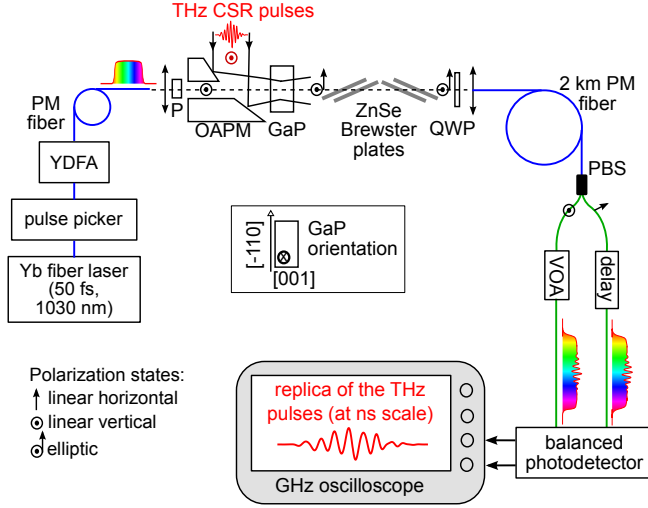


FIG. 2. Experimental setup, combining high sensitivity electro-optic sampling and photonic time-stretch. High sensitivity is obtained by using the four ZnSe plates, using the arrangement proposed in Ref.²². Blue and green lines represent polarization maintaining (PM), and non-polarization maintaining (SM) fibers, respectively. YDFA: Ytterbium-doped fiber amplifier delivering 12 nJ pulses, P: polarizer, OAPM: 50.8 focal length off-axis parabolic mirror. GaP: Gallium Phosphide electro-optic crystal. QWP: quarter-wave plate (oriented at 45 degrees with respect to the figure plane), VOA: variable optical attenuator. PBS: fibered polarizing coupler (the slow axis of the PM fiber is coupled to the VOA port). The two fiber collimators have 11 mm focal length. The vertical and horizontal polarization components are injected in the slow and fast axes of the PM fiber, respectively.

of our amplifier (by a factor 4).

IV. DISCUSSION

A. Increase in signal level

For a given power at the detector's inputs, the signal is expected to increase by a factor (see appendix and reference²²):

$$a = 1/\sqrt{T}, \quad (2)$$

where T is the transmission of the ZnSe plates for the s-polarization. Assuming a refractive index $n = 2.4858$ for ZnSe (at 1030 nm), and perfect Brewster incidence, the transmission of each brewster interface is 48% for the s-polarization, and the increase factor is hence $a = 18.9$.

In the present experiment, the signal enhancement on the photodetectors is lower than this value because the output laser power is ≈ 4 times lower than without ZnSe plates. Hence a factor ≈ 4.8 in signal enhancement (instead of 18.9) is actually obtained. Note however that the increase in signal to noise ratio is higher than this value, because the shot-noise is also lowered.

B. Enhancement of SNR and noise-equivalent input electric field

The sensitivity of this type of detector can be characterized by the input THz signal, which would be equivalent to the measured noise. This noise-equivalent input signal is non-stationary (i.e., its statistical properties depends on time) because the laser power varies with time. This is also complicated by the transfer function of the photonic time-stretch system (see Figure 7 and Appendix B).

It is nevertheless possible to define a simple estimate for the noise level, that can be used for comparison with other setups (and leave detailed analysis of the non-stationary noise for future works). For this, we use data without THz signal and calculate the RMS noise fluctuation estimate over quasi-flat region of the transfer function, up to 300 GHz (see Figure 7). We also assume a flat frequency response for the r_{41} coefficient on this bandwidth. The RMS noise estimated using this definition is displayed in Figure 5.

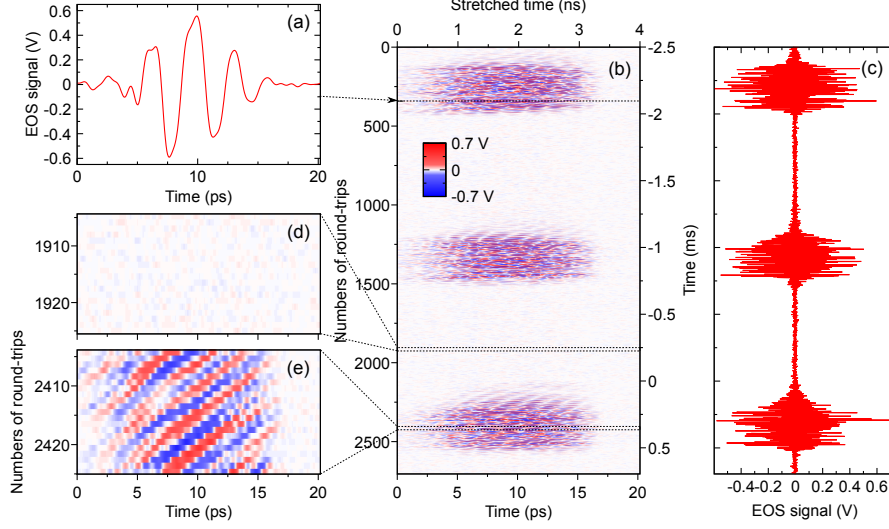
The minimum input noise value is of the order of 1.25 V/cm (RMS, in the crystal) over the 0-300 GHz band, i.e., $2.3 \mu\text{V}/\text{cm}/\sqrt{\text{Hz}}$. This corresponds to an improvement by a factor ≈ 6.75 with respect to the balanced detection data obtained without ZnSe plates.

V. CONCLUSION

Relatively simple photonic time stretch digitizers for free-propagating electric fields can be designed with balanced detection and “near extinction” operation, thus leading to a significant improvement of the signal to noise ratio (by factor 6.7 here). Further increase of the amplifier power output up to the optimal level for the photodiodes (i.e., by a factor 4) should directly lead to the SNR enhancement close to the value $a = 1/\sqrt{T} = 18.9$. In addition, as for scanning EOS²², further increase of the detectivity should be made possible by decreasing the transmission T of the Brewster set plates for the (s) polarization, and increasing the laser power by the same factor.

This technique can be directly applied when the modulation is performed on the birefringence of an electro-optic crystal. Hence – in addition to the detection of THz fields – this also opens new ways for improving the SNR in electron bunch shape measurements systems for accelerators and free-electron lasers. Further relevant works may concern the association of the present scheme with the so-called amplified time-stretch strategy¹⁰ (with the aim to further enhance detectivity), as well as extending the THz detection bandwidth, using e.g., phase diversity^{5,6,34}. Last but not least, reduction of the setup cost may be possible, e.g., by replacing the PM fiber with an SM fiber if a system with circulators can be implemented efficiently³⁵. Applications of this method to digitization of cable-transported signals^{1,4} still remains an open ques-

With ZnSe plates at Brewster angle



Without ZnSe plates at Brewster angle

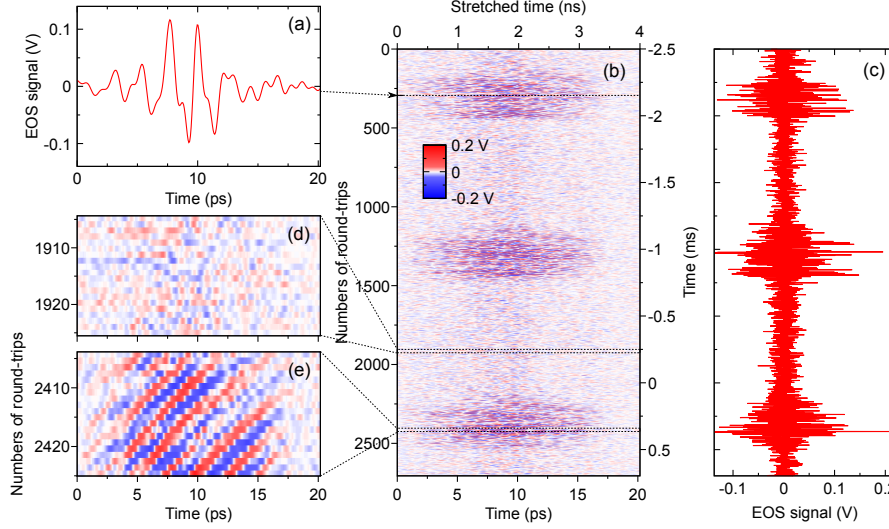


FIG. 3. Single-shot recordings (balanced photodetector voltage) of successive THz coherent pulses (CSR). The upper part corresponds to a recording using the present setup. The lower part corresponds to the setup without sensitivity enhancement system (ZnSe plates). (a): one single shot EOS signal, (b) and (d): series of EOS THz signals $V_n(t)$ over many round-trips n , represented as a colorscale diagram [(d) is a zoom of (b)]. (c): signal at center $V_n(t = 10 \text{ ps})$ versus round-trip number n . Note the difference in SNR ratio between upper and lower data.

tion, as the feasibility can depend on the possibilities to apply the Ahmed-Savolainen-Hamm principle to fibered modulators (e.g., polarization modulators⁴).

VI. ACKNOWLEDGEMENTS

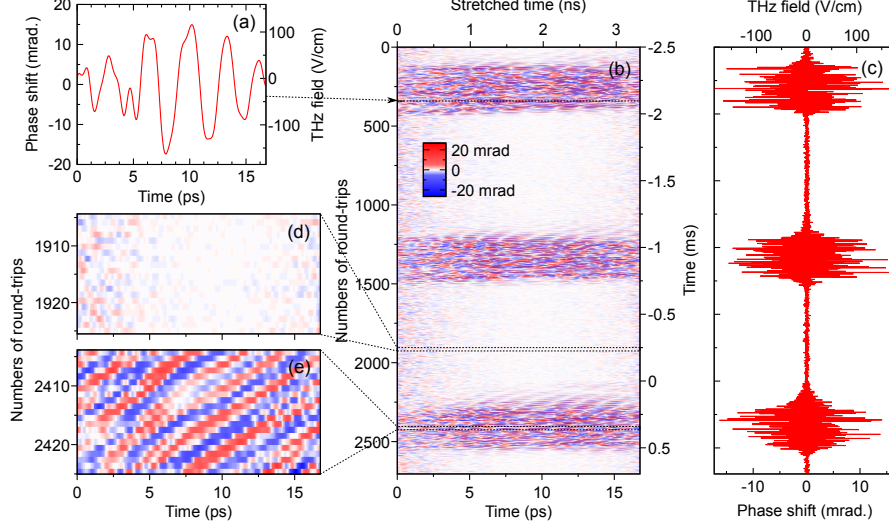
We would like to thank Menlo Systems for important advices. The work has been supported by the BQR of Lille University (2015). The work has also been supported by the Ministry of Higher Education and Research, Nord-Pas de Calais Regional Council and European Regional Development Fund (ERDF) through

the Contrat de Projets État-Région (CPER) 20072013, and the LABEX CEMPI project (ANR-11-LABX-0007). Preparation of the experiment used HPC resources from GENCI TGCC/IDRIS (i2015057057, i2016057057).

Appendix A: Note on the efficiency of balanced detection

Proper adjustment of the delay line is expected to lead to an efficient noise cancellation between the two balanced detector's inputs. This is illustrated in Figure 6 where we represented the noise level (at the balanced detector's output) versus delay, in absence of THz sig-

With ZnSe plates at Brewster angle



Without ZnSe plates at Brewster angle

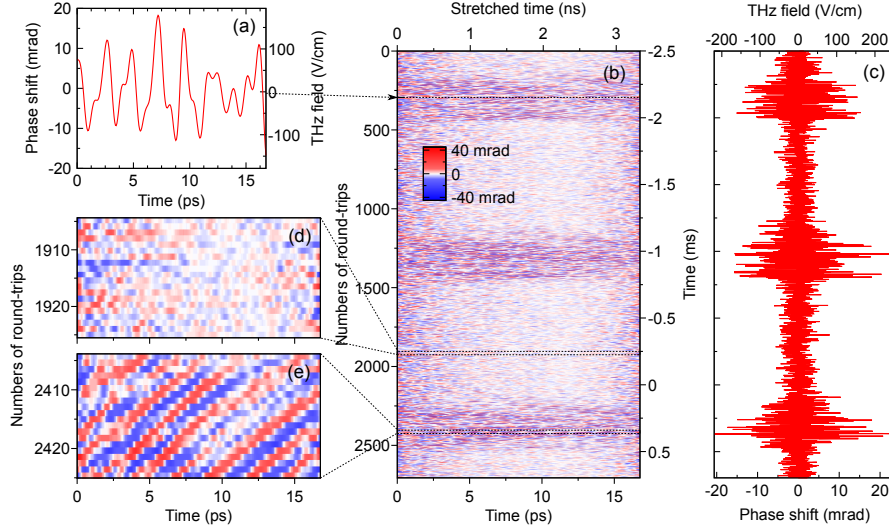


FIG. 4. Estimation of the phase-shift inside the crystal, and of the THz electric field from the data of Figure 3. This estimation assumes a constant electro-optic coefficient $r_{41} = 1 \text{ pm/V}^{33}$ for Gallium Phosphide over the THz signal bandwidth. The 3 dB system bandwidth is 0.4 THz (see Appendix B).

nal. The remaining noise is slightly higher than the “no-signal” detector noise ($\approx 5.8 \text{ mV RMS}$ over the 6 GHz bandwidth). This indicates a satisfying common mode rejection on the whole temporal window defined by the laser pulse duration.

Appendix B: Modeling details

1. Output signal versus input THz electric field

The experimental setup contains two main building blocks, which have been theoretically modeled in previous works. In this appendix, we provide for this particular setup: (i) the calculation of the output signal

for a given phase modulation in the crystal, and (ii) the bandwidth limitation due to the time-stretch (or spectral encoding) strategy.

The EOS principle (Fig. 2) can be divided in two parts: (i) The Pockels effect, that leads to the modulation of the two polarization components injected in the PM fiber (the components are eventually separated by the polarizing beam-splitter), and (ii) the dispersion in the long PM fiber. Based on the corresponding literature on electro-optic sampling and photonic time stretch^{1,3–5}, each part can be modeled in a relatively straightforward way.

The THz electric field $E_{THz}(t)$ induces a birefringence, whose optical axes are oriented at 45 degrees with respect to the laser polarization. In the horizontal-vertical axes

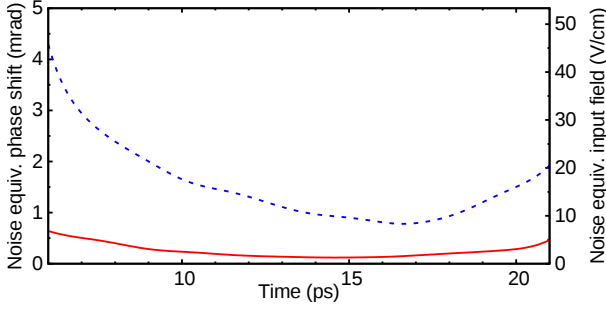


FIG. 5. Input electric field equivalent to the noise level, over a bandwidth of 300GHz. The red (full line) and blue (dashed line) lines correspond to the setup with and without the Brewster plate system, respectively. The left vertical axis corresponds to the THz-induced birefringence phase shift.

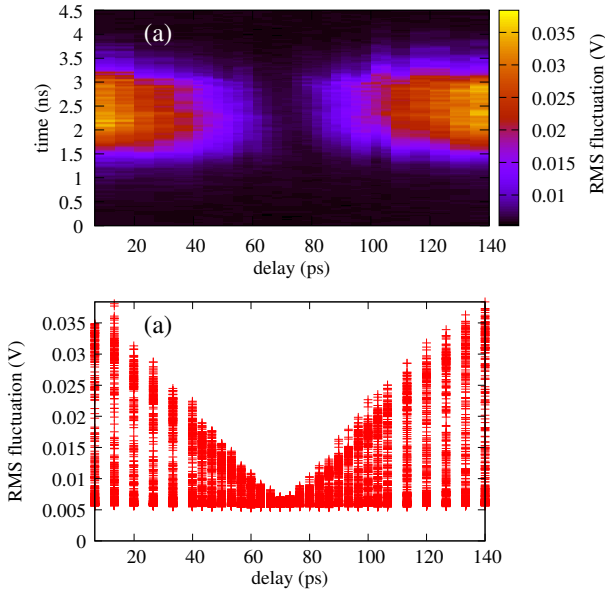


FIG. 6. Measured output noise level (RMS oscilloscope signal in absence of THz pulses), versus delay between the two balanced photodetector inputs (note that the origin of the horizontal axis is arbitrary). (a): noise versus time at oscilloscope input (vertical axis), and delay (horizontal axis). (b): same data projected vertically (i.e., RMS noise levels for each oscilloscope times, versus delay). Laser noise cancellation is clearly visible when the delay line adjustment is at the 70 ps value (i.e., corresponding to zero delay between the two balanced detection signals). Detector noise (in absence of laser) corresponds to ≈ 5.8 mV RMS. Noise is measured on a 6 GHz bandwidth, corresponding to an 1.2 THz limitation in the electro-optic crystal.

frame, the Jones matrix of the electro-optic crystal is³⁶

$$\mathbf{M}_{GaP} = \exp(i\phi_0) \begin{pmatrix} \cos \frac{\Delta\phi}{2} & i \sin \frac{\Delta\phi}{2} \\ i \sin \frac{\Delta\phi}{2} & \cos \frac{\Delta\phi}{2} \end{pmatrix}, \quad (\text{B1})$$

where $\Delta\phi(t)$ represents the relative phase retardation between the two optical axes of the crystal, and ϕ_0 a con-

stant phase shift. Note that, at a given THz frequency³⁶:

$$\Delta\phi(t) = \frac{2\pi d}{\lambda} n_0^3 r_{41} E_{THz}(t), \quad (\text{B2})$$

for the present crystal orientation, with $E_{THz}(t)$ the THz field inside the crystal, r_{41} the relevant electro-optic coefficient at the considered THz frequency, λ the laser wavelength in vacuum, n_0 the crystal refractive index, and d its thickness. Here: $\lambda = 1030$ nm, $n_0 = 3.11$ ³⁷, and $r_{41} \approx 1$ pm/V³³.

At the input of the PM fiber, the two laser polarization components E_1 and E_2 are: (see, e.g., Ref.²² for details):

$$\begin{pmatrix} E_x^{in}(t) \\ E_y^{in}(t) \end{pmatrix} = \frac{\sqrt{T}E_0(t)}{\sqrt{2}} \begin{pmatrix} \cos \frac{\Delta\phi(t)}{2} - \frac{1}{\sqrt{T}} \sin \frac{\Delta\phi(t)}{2} \\ i \left[\cos \frac{\Delta\phi(t)}{2} + \frac{1}{\sqrt{T}} \sin \frac{\Delta\phi(t)}{2} \right] \end{pmatrix}, \quad (\text{B3})$$

where we have omitted the global constant phase shift due to propagation, T is the transmittance of the Brewster plate set for the s-polarization (perfect transmission is assumed for the other polarization). $E_0(t)$ represents the complex envelope of the chirped laser pulse just before the crystal.

Then each polarization component experiences dispersion in the PM fiber. Neglecting high-order dispersion, losses, and nonlinearity, the two components $E_x(z, t)$ and $E_y(z, t)$ satisfy the following propagation equation:

$$\frac{\partial E_x}{\partial z} = -i \frac{\beta_{2x}}{2} \frac{\partial^2 E_x}{\partial t^2} \quad (\text{B4})$$

$$\frac{\partial E_y}{\partial z} = -i \frac{\beta_{2y}}{2} \frac{\partial^2 E_y}{\partial t^2}, \quad (\text{B5})$$

where β_{2x} and β_{2y} are the dispersions for each polarization components of the PM fiber. However, the difference of dispersion has negligible effect in the present experiment. Hence we consider that each component propagates with the same dispersion $\beta_{2x} = \beta_{2y} = \beta_2$ and a same equivalent length $L_x = L_y = L$.

Simulation of the EOS system hence requires the integration of Eqns. (B4,B5), where the initial condition (at $z = 0$) is given by Eq. (B3). Then, we easily deduce the powers $|E_x|^2$ and $|E_y|^2$ on the two balanced photodiodes.

2. Bandwidth limitations

The frequency response can be studied by computing the complex amplitude of the balanced signal, when the input signal is sinusoidal:

$$\Delta\phi(t) = a_m \cos 2\pi f_m t. \quad (\text{B6})$$

This can be performed by numerically after integrating Eqns. (B4,B5), using Eq. (B3) as the initial condition. Furthermore, analytical expressions for the transfer function may also be obtained. The situation described by Eq. B3 is formally analog to the modulation by a Mach-Zehnder modulation with zero chirp³, and thus we expect

the transfer function to be identical:

$$H(f_m) = \cos \left(2\pi^2 \beta_2 \frac{L_2}{M} f_m^2 \right) \quad (\text{B7})$$

$$\approx \cos \left(2\pi^2 \beta_2 L_1 f_m^2 \right), \quad (\text{B8})$$

assuming a_m small and M large. $H(f_m)$ is the complex amplitude of the balanced detection signal, normalized to its value at $f_m = 0$ (and where a global constant phase shift has been omitted). The transfer function is represented in Figure 7 with the parameters of the experiment. $|H(f_m)|$ presents a fading phenomenon, which is characteristic of photonic time-stretch, and whose cutoff frequency depends on the length of the fiber (L_1). The first zero is located at:

$$f_{m0} \approx \frac{1}{\sqrt{4\pi\beta_2 L_1}}. \quad (\text{B9})$$

In time domain, this fading corresponds the well-known trade-off between the resolution τ_R and time window τ_w of the analysis (see e.g., Ref.¹⁵, as well as Ref.¹⁶ for a detailed analysis):

$$\tau_R = O(\sqrt{\tau_w \times \tau_{L0}}), \quad (\text{B10})$$

where τ_{L0} is the unstretched laser pulse duration, and $\tau_w \approx \beta_2 L_1$ if $\tau_w \gg \tau_{L0}$.

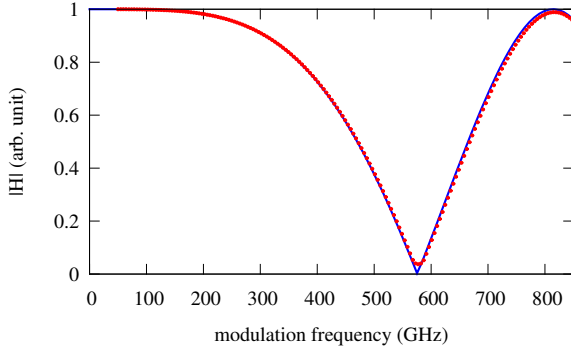


FIG. 7. Transfer function (more precisely $|H(f_m)|$). Red dots: numerical result using integration of Eqns. (B4,B5), with $\Delta\phi(t) = a_m \cos 2\pi f_m t$. Blue curve: Analytic result using Eq. (B8). $\beta_2 = 24 \text{ ps}^2/\text{km}$, $L_1 = 10 \text{ m}$, $L_2 = 2000 \text{ m}$, $a_m = 0.01$. The initial laser pulse is Gaussian, with 40 fs duration (FWHM).

3. Computation of the THz electric field from experimental data

In the frequency region where the transfer function H is close to 1 (i.e., over the detector bandpass), and assuming that r_{41} is almost constant, we can easily deduce the terahertz electric field evolution $E_{THzn}(t)$, and the birefringence phase-shift inside the crystal $\Delta\phi_n(t)$ at electron

bunch passage n from the experimental data. For small values of $\Delta\phi_n(t)$:

$$\Delta\phi_n(t) \approx \frac{1}{a} \frac{V_{1n}(t) - V_{2n}(t)}{V_1^0(t) + V_2^0(t)} \quad (\text{B11})$$

$$E_{THzn}(t) = \frac{\lambda}{2\pi d n_0^3 r_{41}} \Delta\phi_n(t), \quad (\text{B12})$$

where $V_{1n}(t) - V_{2n}(t)$ is the raw balanced detection signal (corresponding to Figure 3), V_1^0 and V_2^0 are the individual signals corresponding to each detector without THz field (V_1^0 and V_2^0 are identical). a is the signal enhancement factor defined above (and $a = 1$ without ZnSe plates). Data presented in Figures 4 and 5 are obtained using these assumptions (in particular, we did not attempt to deconvolve the data using informations on the transfer function H).

- ¹F. Coppinger, A. Bhushan, and B. Jalali, IEEE Trans. on Microwave Theory and Techniques **47**, 1309 (1999).
- ²K. Goda and B. Jalali, Nature Photonics **7**, 102 (2013).
- ³Y. Han and B. Jalali, J. Lightwave Technology **21**, 3085 (2003).
- ⁴J. Wong, H. Lam, R. Li, K. Li, V. Wong, P. Lim, S. Aditya, P. Shum, S. Xu, K. Wu, and C. Ouyang, J. Lightwave Tech. **29**, 3099 (2011).
- ⁵Y. Han, O. Boyraz, and B. Jalali, IEEE Trans. on Microwave Theory and Techniques **53**, 1404 (2005).
- ⁶D. Chang, H. Erlig, M. Oh, C. Zhang, W. Steier, L. Dalton, and H. Fetterman, IEEE Photonics Technol. Lett **12**, 537 (2000).
- ⁷Roussel, E. Evain, C. L. Parquier, M. Szwaj, C. Bielawski, S. Manceron, L. Brubach, J-B, Tordeux, M-A, Ricaud, J-P, Cassinari, L. Manceron, and P. Roy, Scientific Reports **5**, 10330 (2015).
- ⁸E. Roussel, Thèse de l'Université de Lille, France (2014, in english).
- ⁹E. Roussel, C. Evain, S. Szwaj, A. B. S. Bielawski, N. Hiller, A.-S. Müller, P. Schönfeldt, and J. Steinmann, Electro-Optical Measurements of the Longitudinal Bunch Profile in the Near-Field on a Turn-by-Turn Basis at the Anka Storage Ring, Proceedings of IBIC, Melbourne, Australia, MOPB006 (2015).
- ¹⁰D. Solli, J. Chou, and B. Jalali, Nature Photonics **2**, 48 (2008).
- ¹¹J. A. Valdmanis and G. Mourou, Quantum Electronics, IEEE Journal of **22**, 69 (1986).
- ¹²Q. Wu and X. Zhang, Applied Physics Letters **67**, 3523 (1995).
- ¹³A. Nahata, A. S. Weling, and T. F. Heinz, Applied Physics Letters **69**, 2321 (1996).
- ¹⁴Z. Jiang and X.-C. Zhang, Appl. Phys. Letters **72**, 1945 (1998).
- ¹⁵F. Sun, Z. Jiang, and X.-C. Zhang, Applied Physics Letters **73**, 2233 (1998).
- ¹⁶X.-Y. Peng, O. Willi, M. Chen, and A. Pukhov, Optics express **16**, 12342 (2008).
- ¹⁷I. Wilke, A. M. MacLeod, W. A. Gillespie, G. Berden, G. M. H. Knippels, and A. F. G. van der Meer, Phys. Rev. Lett. **88**, 124801 (2002).
- ¹⁸U. Schmidhammer, V. De Waele, J.-R. Marques, N. Bourgeois, and M. Mostafavi, Applied Physics B **94**, 95 (2009).
- ¹⁹I. Katayama, H. Shimosato, M. Bito, K. Furusawa, M. Adachi, M. Shimada, H. Zen, S. Kimura, N. Yamamoto, M. Hosaka, M. Katoh, and M. Ashida, Applied Physics Letters **100**, 111112 (2012), <http://dx.doi.org/10.1063/1.3694049>.
- ²⁰F. Müller, P. Peier, V. Schlott, B. Steffen, T. Feurer, and P. Kuske, Phys. Rev. ST Accel. Beams **15**, 070701 (2012).
- ²¹N. Hiller, A. Borysenko, E. Hertle, E. Huttel, V. Judin, B. Kehrer, S. Marsching, A.-S. Müller, M. Nasse, A. Plech, M. Schuh, and S. Smale, Electro-optical bunch length measurements at the ANKA storage ring, Proceedings of the 2013 Particle Accelerator Conference, Shanghai, China, MOPME14 (2013).

- ²²S. Ahmed, J. Savolainen, and P. Hamm, Review of Scientific Instruments **85**, 013114 (2014).
- ²³J. Savolainen, S. Ahmed, and P. Hamm, Proc. Natl. Acad. Sci. U.S.A. **110**, 20402 (2013).
- ²⁴C. Evain, J. Barros, A. Loulergue, M. A. Tordeux, R. Nagaoka, M. Labat, L. Cassinari, G. Creff, L. Manceron, J. B. Brubach, P. Roy, and M. E. Couprie, EPL **98**, 40006 (2012).
- ²⁵J. Barros, C. Evain, L. Manceron, J.-B. Brubach, M.-A. Tordeux, P. Brunelle, L. Nadolski, A. Loulergue, M.-E. Couprie, S. Bielawski, C. Szwaj, and P. Roy, Review of Scientific Instruments **84**, 033102 (2013).
- ²⁶J. Barros, C. Evain, E. Roussel, L. Manceron, J.-B. Brubach, M.-A. Tordeux, M.-E. Couprie, S. Bielawski, C. Szwaj, M. Labat, *et al.*, Journal of Molecular Spectroscopy **315**, 3 (2015).
- ²⁷S. Tammaro, O. Pirali, P. Roy, J.-F. Lampin, G. Ducournau, A. Cuisset, F. Hindle, and G. Mouret, Nature communications **6** (2015).
- ²⁸P. Gaal, M. Raschke, K. Reimann, and M. Woerner, Nature Photonics **1**, 577 (2007).
- ²⁹Z. Jiang, F. Sun, Q. Chen, and X.-C. Zhang, Applied Physics Letters **74**, 1191 (1999).
- ³⁰X. Shi-Xiang and C. Hua, Chinese Physics Letters **25**, 152 (2008).
- ³¹B. Steffen, V. Arsov, G. Berden, W. Gillespie, S. Jamison, A. M. MacLeod, A. Van Der Meer, P. Phillips, H. Schlarb, B. Schmidt, *et al.*, Physical Review Special Topics-Accelerators and Beams **12**, 032802 (2009).
- ³²P. Roy, M. Rouzières, Z. Qi, and O. Chubar, Infrared Physics and Technology **49**, 139 (2006).
- ³³D. Nelson and E. Turner, Journal of Applied Physics **39**, 3337 (1968).
- ³⁴A. Tarighat, S. Gupta, A. H. Sayed, and B. Jalali, Journal of lightwave technology **25**, 1580 (2007).
- ³⁵A. Fard, B. Buckley, and B. Jalali, Photonics Technology Letters, IEEE **23**, 947 (2011).
- ³⁶S. Casalbuoni, H. Schlarb, B. Schmidt, P. Schmüser, B. Steffen, and A. Winter, Physical Review Special Topics-Accelerators and Beams **11**, 072802 (2008).
- ³⁷D. Parsons and P. Coleman, Applied optics **10**, 1683.1 (1971).